Synthesis and Characterization of Fe^{3+} and CeO_2 Co-decorated NiOOH Electrocatalysts Supported by Nickel Foam for the Oxygen Evolution Reaction

Haoyu Zhang, Jingguang Du, Dongfang Niu, Shuozhen Hu[*] and Xinsheng Zhang[*]

State Key Laboratory of Chemical Engineering, East China University of Science and Technology, Shanghai, 200237, China
[*]E-mail: shuozhen.hu@ecust.edu.cn, xszhang@ecust.edu.cn

Inexpensive and non-noble metal catalysts for the oxygen evolution reaction (OER) with high activity and stability must be developed to enhance water electrolysis for hydrogen production. Herein, Fe^{3+} dopants and flower-shaped CeO_2-decorated NiOOH catalysts are synthesized, and the synergetic effect of Fe^{3+} dopants and CeO_2 are investigated. The presence of both Fe^{3+} dopants and CeO_2 produces more NiOOH species and more oxygen vacancies in the NiOOH structure as measured by X-ray photoelectron spectroscopy. Electrochemical measurements illustrate that the increase in oxygen vacancies in NiOOH significantly increases the conductivity and activity of the catalyst and reduces the OER overpotential. Among the catalysts studied in this research, CeO_2-NiFeOH/NF, which is modified by both Fe^{3+} dopants and CeO_2, hosts the highest number of oxygen vacancies. It also has the lowest overpotential (280 mV), the highest current density, and excellent stability with high performance for the OER.

1. INTRODUCTION

The green production of hydrogen as a non-carbon energy source is a popular research topic. Water electrolysis driven by renewable energies is considered to be the most clean and efficient method for hydrogen production. However, the oxygen evolution reaction (OER), with a theoretical potential of 1.23 V, is the crucial anodic half reaction in water electrolysis [1-3]. A high overpotential is always required for the OER to proceed. Many studies have focused on developing efficient and durable OER catalysts. It is well known that IrO_2 and RuO_2 have remarkable catalytic performances for the OER. However, the high cost and low contents of Ir and Ru on Earth restrict their application [4-6]. Currently, many efforts have been devoted to develop transition-metal-based catalysts.

In alkaline electrolytes, oxides and hydroxides of transition metals, such as Ni, Co, Fe, and Mn, are good candidates for efficient OER catalysts [7-13]. Among metal oxides and hydroxides, NiOOH shows remarkable activity for OER because it contains a high oxidation state of Ni, i.e., $Ni^{III/IV}$, which is the active site for the OER [14-17]. NiOOH is perfect for the OER because it contains Ni^{3+} in the structure and the occupation of the Ni^{3+} e_g empty state is approximately 1.2 [18]. Consequently, the bond between Ni^{3+} and OH^- is sufficiently strong for O-H bond breaking and O-O bond formation and follows the Sabatier principle for catalyst design [19,20]. However, the activity and conductivity of pure NiOOH are still insufficient for the OER.

To further improve the activity and conductivity of NiOOH, many efforts have been made to dope transition metals [21-22]. Qi et al. found that after doping with 15% of Fe, the onset potential of OER decreased to 1.55 V at 10 mA cm^2 [23]. The improvement is because Fe dopants have a partial-charge-transfer activation effect on Ni, resulting in enhanced electrical conductivity of NiOOH [24]. Moreover, the adsorption energy of the intermediate species (*OH) on the surface of Fe-doped NiOOH is 1.60 eV, which is lower than that of pure NiOOH (1.84 eV). As a result, the conversion of *OH to *O species in the OER is easier [25].

In addition to doping transition metals, introducing metal oxides to NiOOH is another effective method to improve the catalytic performance of NiOOH for the OER [26-27]. CeO_2 has gained widespread attention in both photocatalysis and electrochemical systems for the OER due to its large number of oxygen vacancies and its redox ability [28]. Li et al. synthesized $FeOOH/CeO_2$ as an efficient OER electrocatalyst [29]. They illustrated that $FeOOH/CeO_2$ has a lower adsorption energy of OH^- than FeOOH and CeO_2, which enhances its electrocatalytic activity towards OER. Du and coworkers [30] used CeO_2 to increase the amount of active species of $Ni(OH)_2$ on carbon foam, which also improves the OER activity.

Some studies modified NiOOH by both transition metal dopants and metal oxides and observed much better OER performance [31-32]. In contrast, Fe^{3+} dopants and CeO_2 co-modified NiOOH have rarely been studied. The effects of Fe^{3+} dopants and CeO_2 on NiOOH have not been comprehensively investigated, nor have their effects on the electrochemical activity towards OER.

In this work, the synergetic effect of Fe^{3+} dopants and CeO_2 on the NiOOH structure and its catalytic activity towards OER are studied. Nickel foam (NF) is used as the support due to its high surface area and good structural stability [33-34]. CeO_2-NiFeOH/NF, CeO_2/NF-heat, NiFeOH/NF, and NF-heat are synthesized and analysed. Based on X-ray photoelectron spectroscopy (XPS) and electrochemical analysis, the Fe^{3+} and CeO_2 co-modified CeO_2-NiFeOH/NF catalyst has the largest number of oxygen vacancies, exhibits the lowest OER overpotential and the highest current density.

2. EXPERIMENTAL

2.1 Synthesize of NF-supported NiOOH catalysts modified by Fe^{3+} dopants and CeO_2

CeO_2-NiFeOH/NF were synthesized as follows. Nickel foams (NFs) (Kun Shan Jia Yi Sheng Electronics Co., Ltd) with a size of 10 * 10 mm were first sonicated in acetone for 10 minutes to remove

impurities on the surface followed by successive rinsing with ethanol and Millipore® water (18.3 MΩ). The cleaned NF sheets were then dipped into a 50 mmol L^{-1} $FeCl_3$ (AR, Shanghai Titan Scientific Co., Ltd) aqueous solution for 10 seconds and were heated at 300 ºC for 2 hours in air atmosphere to produce NiFeOH/NF. To deposit CeO_2, NiFeOH/NF was immersed in 0.05 mol L^{-1} $Ce(NO_3)_3$ solution (99.5%, Shanghai Macklin Biochemical Co., Ltd) under ultrasonication. A 28% NH_4OH solution (AR, Shanghai Titan Scientific Co., Ltd) was added dropwise into the $Ce(NO_3)_3$ solution that contained NiFeOH/NF until the pH of the solution reached 10. Finally, the CeO_2-NiFeOH/NF samples were removed and dried in a vacuum oven at 80 ºC. NiFeOH/NF samples were synthesized with the same procedure without the deposition of CeO_2. CeO_2/NF-heat samples were produced according to the same heating method without Fe treatment. As a comparison, NF-heat samples without Fe and CeO_2 modifications were also prepared using the same annealing method.

2.2 Physical Characterization

The morphology and elemental distribution of all NF supported catalysts were detected by field emission scanning electron microscopy equipped with energy dispersive spectrometer (FESEM-EDS) (Zeiss Merlin Compact, Oxford X-50). X-ray photoelectron spectroscopy (XPS) was performed on an ESCALAB 250 instrument to analyse the chemical states of all the samples. All spectra were calibrated against the C 1s peak at 284.6 eV. The crystalline structures of the synthesized samples were characterized by X-ray diffraction (Bruker D8 diffractometer) with Cu K_α radiation ($\lambda = 0.15418$ nm).

2.3 Electrochemical Measurements

All electrochemical measurements were performed on an Autolab workstation (PGSTAT 302N) connected to a standard three-electrode system at room temperature. The modified nickel foam samples were used as the working electrode. The Ag/AgCl (3.5 M KCl) electrode and the Pt wire were used as the reference electrode and counter electrodes, respectively. Linear sweep voltammetry (LSV) was used to detect the OER activity of catalysts at a scan rate of 5 mV s^{-1}. To keep the electrode surface in a relatively stable state, before each LSV measurement, several cyclic voltammetry (CV) cycles were operated at a scan rate of 50 mV s^{-1} between 1.2 and 2.0 V until the redox peaks of nickel and the oxygen evolution currents did not change. Before each electrochemical measurement, the electrolyte was saturated with high-purity O_2 gas (99.999%). The voltammograms were calibrated with iR drop compensation manual-matically after the measurements. The electrochemical impedance spectra (EIS) were recorded on the workstation at 0.5 V with a frequency range from 100 KHz to 50 mHz. All potentials reported in this work were calibrated versus the reversible hydrogen electrode (RHE) using the following equation: $E_{RHE} = E_{Ag/AgCl} + 0.21 + 0.059 * pH$ (V), where E_{RHE} is the potential referred to the RHE and $E_{Ag/AgCl}$ is the measured potential against the Ag/AgCl reference electrode.

3. RESULTS AND DISCUSSION

3.1 Physical characterization of NF-supported NiOOH catalysts modified by Fe^{3+} dopants and CeO_2
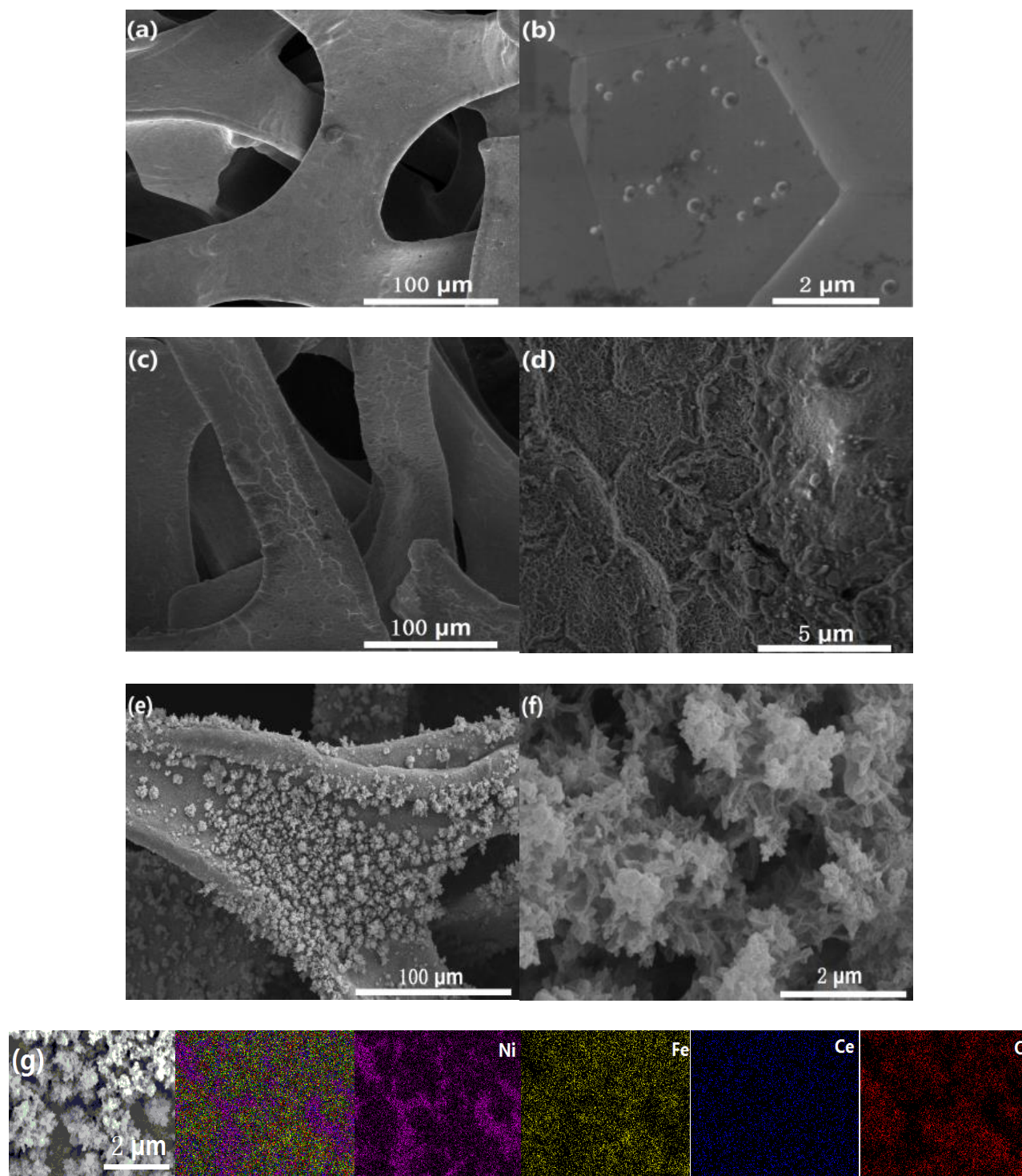

Figure 1. SEM of (a)-(b) NF-heat, (c)-(d) NiFeOH/NF, (e)-(f) CeO_2-NiFeOH/NF, and (g) EDS elemental maps of CeO_2-NiFeOH/NF.

The surface morphologies of NF-heat, NiFeOH/NF and CeO_2-NiFeOH/NF were characterized by field emission scanning electron microscopy (FESEM), as shown in Figure 1. As Figure 1(a)-(b)

shows, the surface of NF-heat is smooth and clean. After dipping the NF-heat samples into the $FeCl_3$ solution, the surfaces of the NiFeOH/NF catalysts become rough and wrinkled. This is because the standard electrode potential of Fe^{3+}/Fe (-0.04 V vs. RHE) is higher than that of Ni^{2+}/Ni (-0.25 V vs. RHE). There is an exchange reaction between Fe^{3+} and Ni that results in the formation of a rough and wrinkled surface film on the NiFeOH/NF sample (shown in Figure 1(c)-(d)). For the CeO_2-NiFeOH/NF catalyst, as shown in Figure 1(e)-(f), flower-shaped CeO_2 particles with high surface areas are uniformly dispersed on the NiFeOH/NF surface. Along with FESEM, elemental mapping results of the CeO_2-NiFeOH/NF catalyst support that the Fe, Ce, and O elements are uniformly dispersed on the NF surface (shown in Figure 1(g)).
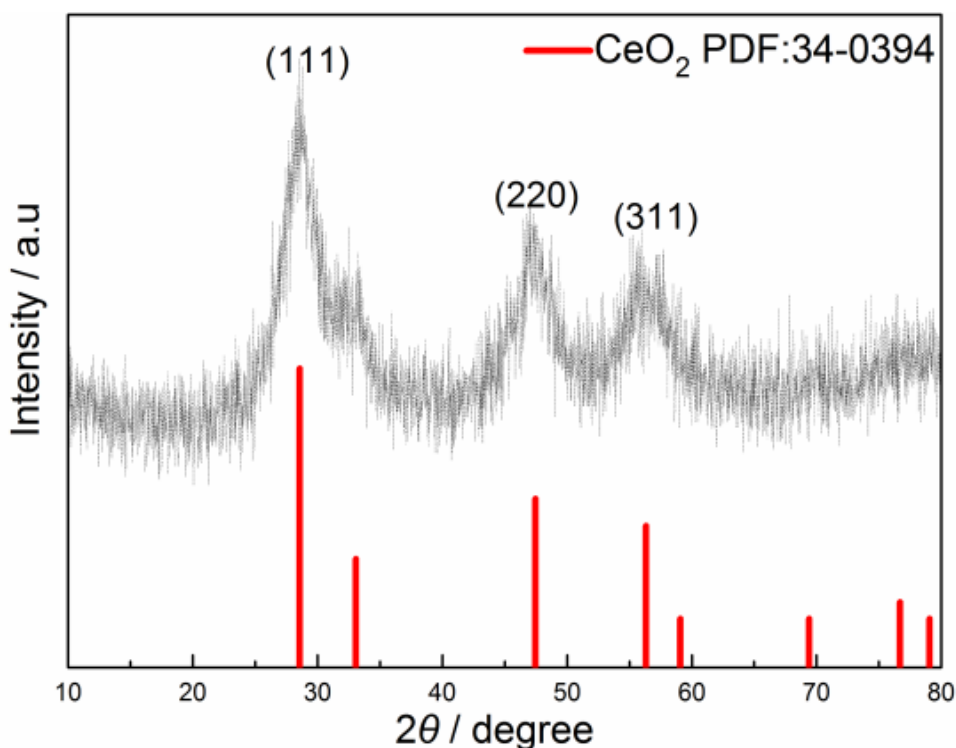

Figure 2. XRD pattern of CeO_2 scratched from CeO_2-NiFeOH/NF and standard XRD PDF card of CeO_2 (No. 34-0394)

To analyse the crystalline structures of the catalysts, X-ray diffraction (XRD) was used. Only metallic nickel is detected for all the samples in the presence of NF. All the XRD signals belonging to CeO_2, Fe, and oxidized nickel species are hindered by the signal from metallic nickel, which is not shown here. This suggests that the Ni-Fe layer and the layer of CeO_2 particles on NF (shown in Figure 1(c)-(f)) are very thin. Thus, the crystalline structure of CeO_2 is detected by XRD by scratching the CeO_2 nanoparticles off the CeO_2-NiFeOH/NF surface. The XRD pattern of CeO_2 shows the CeO_2(111), CeO_2(220), and CeO_2(311) planes at 28.6°, 47.5°, and 56.3° (shown in Figure 2), respectively, indicating that a CeO_2 cubic fluorite structure is formed (JCPDS No. 34-0394).

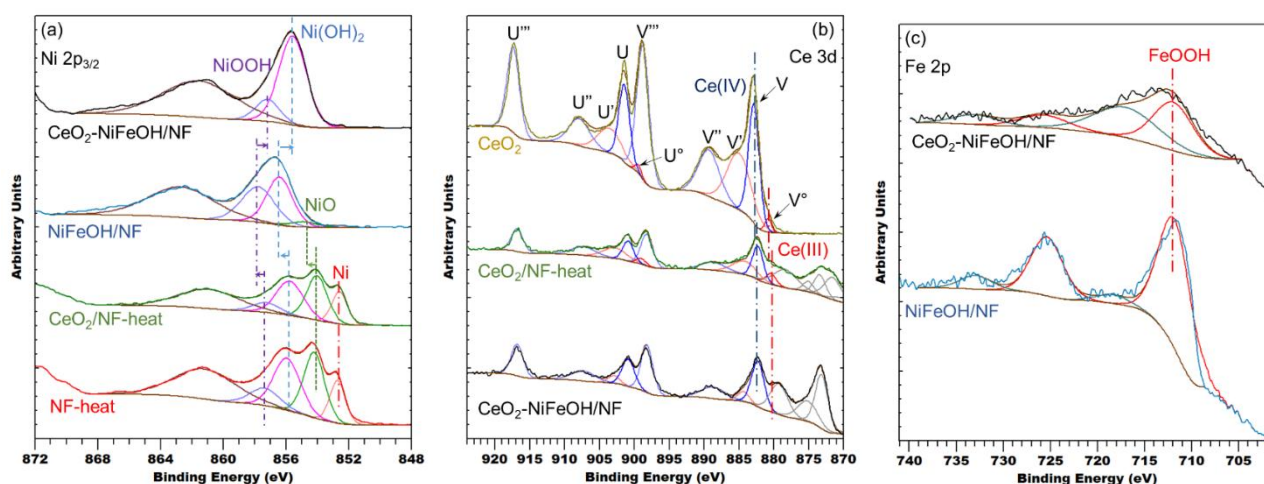*3.2 The effect of Fe^{3+} dopants and CeO_2 on the NiOOH structure*

Figure 3. Core-level XPS spectra of all the samples: (a) Ni $2p_{3/2}$, (b) Ce 3d, and (c) Fe 2p

To further investigate the effect of Fe^{3+} dopants and CeO_2 on the structure of NiOOH, X-ray photoelectron spectroscopy (XPS) was used. Because of the overlap between the Ni $2p_{1/2}$ and Ce $3d_{5/2}$ peaks at approximately 880 eV, only Ni $2p_{3/2}$ was deconvoluted.

As illustrated in Figure 3(a), the core-level XPS Ni $2p_{3/2}$ spectra of the NF-heat sample can be deconvoluted into five distinct peaks. The peaks at approximately 852.7 eV, 854.2 eV, 855.9 eV, and 857.4 eV belong to Ni, NiO, Ni(OH)$_2$, and NiOOH, respectively, whereas the peak at approximately 861.0 eV represents the shake-up satellite of Ni $2p_{3/2}$ [23, 35]. Thus, a layer of oxidized nickel with approximately 15.91% of NiOOH is formed on the NF surface after the heat treatment in air. The detection of metallic Ni indicates that the oxidized nickel layer is thinner than 10 nm, which is in consistent with the absence of nickel oxide and nickel hydroxide signals in the XRD measurements.

Similar to NF-heat, the core-level XPS Ni $2p_{3/2}$ spectra of CeO_2/NF-heat can also be deconvoluted into five peaks, namely, Ni, NiO, Ni(OH)$_2$, NiOOH, and a satellite without a noticeable peak binding energy (BE) shift (shown in Table S1). However, the concentration of NiOOH is slightly reduced from 15.91% to 12.98%. More Ni(OH)$_2$ and NiO are detected. The opposite concentration change suggests that a small number of oxygen vacancies and OH vacancies are formed in the NiOOH structure after depositing CeO_2 on the NF-heat surface. The core-level Ce 3d XPS spectra are also detected for CeO_2/NF-heat and CeO_2 powder. As shown in Figure 3(b), the components are labelled as V and U for the spin orbits $3d_{5/2}$ and $3d_{3/2}$, respectively. V, V″, V‴, U, U″, and U‴ belong to Ce^{4+}, while V°, V′, U°, and U′ refer to Ce^{3+} [36-37]. The presence of Ce^{3+} in the CeO_2 powder is because CeO_2 contains oxygen vacancies in the CeO_2 structure [28, 38-39]. After depositing CeO_2 particles onto the NF surface, the Ce 3d peak of Ce^{3+} is not shifted, but the concentration of Ce^{3+} is slightly reduced from 24.52% to 21.88% (details are listed in Table S2). Meanwhile, the concentration of Ce^{4+} increases. The opposite concentration changes of Ce^{3+} and Ce^{4+} suggest that fewer oxygen vacancies exist in the CeO_2 structure after depositing CeO_2 on NiOOH. The Ni $2p_{3/2}$ and Ce 3d XPS spectra for CeO_2/NF-heating indicate that oxygen vacancies and OH vacancies are produced in the NiOOH structure with the

modification of CeO_2.

However, for the NF samples modified with Fe, the XPS signal for metallic nickel nearly disappears, indicating that the rough surface of the NiFeOH/NF catalyst (shown in Figure 1(e)-(f)) is thicker than 10 nm. In addition, the concentration of NiO obtained from Ni $2p_{3/2}$ is significantly reduced from 41.55% to only 5.53%. The NiOOH concentration of NiFeOH/NF (46.04%) is approximately three times higher than that of the NF-heat sample (15.91%). Moreover, the peak positions of $Ni(OH)_2$ and NiOOH for NiFeOH/NF shift to higher BE by approximately 0.4 eV, while the peak shift of NiO is approximately 0.7 eV compared to NF-heat. All these changes in XPS results suggest that Ni with a high oxidation state is produced from NiO by Fe, which is consistent with the literature results [23-25]. As shown in Figure 3(c), the structure of Fe in NiFeOH/NF is FeOOH [40], indicating that Fe^{3+} is doped into NiOOH. The higher BE shift of NiOOH in NiFeOH/NF proves that there is a strong electronic interaction between doped Fe^{3+} and Ni atoms. It is rationalized that Fe^{3+} with high electronegativity (1.96) can increase the valence state of surrounding Ni atoms [25] and thus shift the Ni $2p_{3/2}$ peak to higher BE and generate more NiOOH species.

Through careful comparison and analysis of the XPS spectra (Figure 3(a)), the peak position of $Ni(OH)_2$ (855.6 eV) and NiOOH (857.2 eV) for CeO_2-NiFeOH/NF shift to lower BE compared to those of NiFeOH/NF (856.4 eV and 857.8 eV, respectively). In addition, higher concentrations of $Ni(OH)_2$ (75.91%) and lower concentrations of NiOOH (18.50%) are formed on the surface of CeO_2-NiFeOH/NF than on NiFeOH/NF. Both the concentration changes and BE shifts of $Ni(OH)_2$ and NiOOH suggest that more oxygen vacancies are formed in the NiOOH structure in the CeO_2-NiFeOH/NF sample. On the other hand, as Figure 3(b) shows, the increase in the Ce^{4+} concentration and the absence of the $V°$ peak for Ce^{3+} indicate that more Ce^{4+} is formed and fewer oxygen vacancies exist in the CeO_2 structure of the CeO_2-NiFeOH/NF sample than in CeO_2 powder or CeO_2/NF-heat. Specific locations and contents of all elements are listed in Tables S1-S2. The opposite concentration change of NiOOH and $Ni(OH)_2$ and the absence of the Ce^{3+} peak in the Ce 3d XPS for the CeO_2-NiFeOH/NF sample suggest that in the presence of both Fe^{3+} and CeO_2, more lattice oxygen is removed from NiOOH, leaving oxygen vacancies in NiOOH.

Based on the XPS analysis of all NF-supported samples, Fe^{3+} dopants are important to convert NiO to NiOOH, whereas CeO_2 aids the formation of oxygen vacancies. With the presence of both Fe^{3+} dopants and CeO_2, the largest number of oxygen vacancies is formed in the NiOOH structure.

3.3 Effect of Fe^{3+} dopants and CeO_2 on NiOOH electrocatalytic activity and stability towards oxygen evolution reaction

The oxygen evolution reaction (OER) performances of samples were evaluated by linear sweep voltammetry (LSV) in alkaline solution (1 M NaOH, pH = 14) with a standard three-electrode system at a scan rate of 5 mV s^{-1} from 0 to 1 V vs Ag/AgCl. As Figure 4(a) shows, the NF-heat sample exhibits an overpotential of 390 mV at a current density of 10 mA cm^{-2}. After depositing CeO_2 nanoparticles on the NF surface to form CeO_2/NF-heat, a slight negative shift of overpotential (370 mV) and an increase in current density are obtained (increased from approximately 20 mA cm^{-2} to 30 mA cm^{-2} at 1.7 V). Based on the XPS results of CeO_2/NF-heat, NF-heat and CeO_2, more oxygen vacancies are generated in the

NiOOH structure. As Du et al. [30] suggested, the more oxygen vacancies there are in the catalyst, the more active sites and higher electronic and ionic conductivity the catalysts have. Consequently, the OER activity of CeO$_2$/NF-heat is improved.
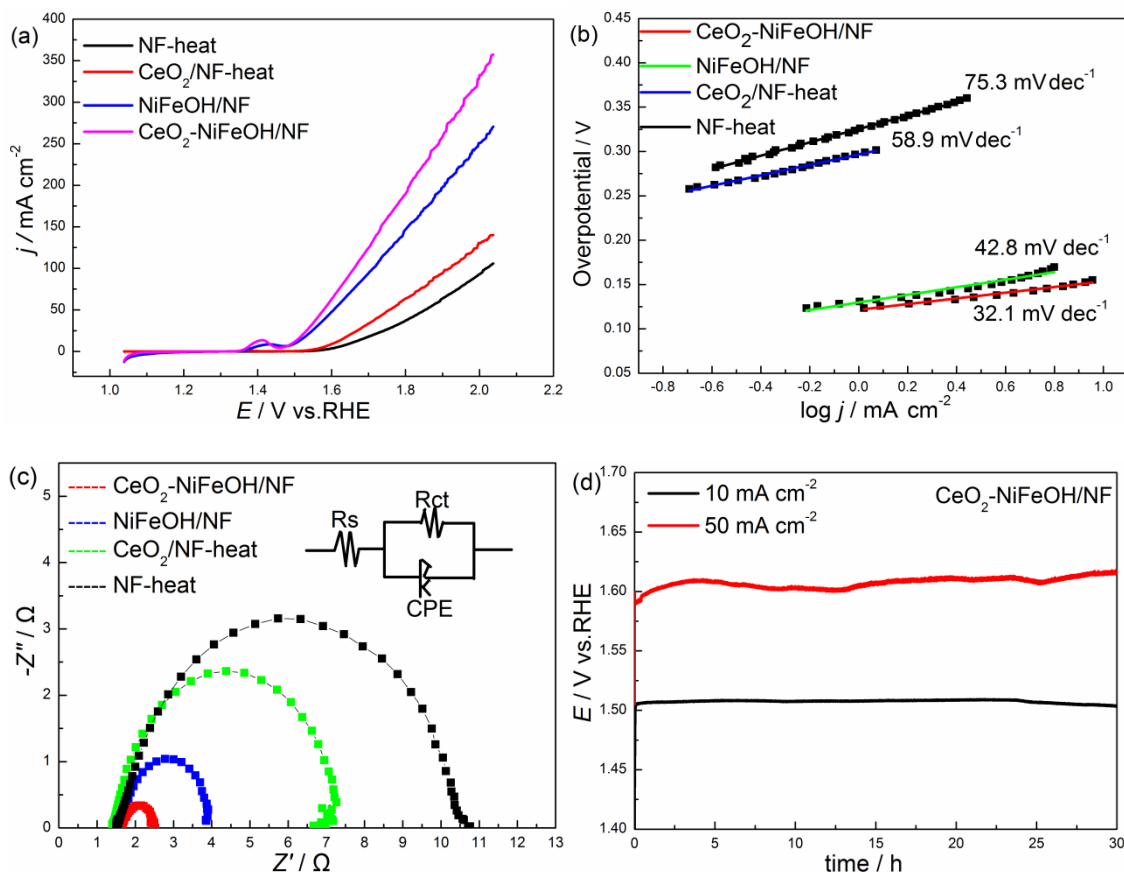

Figure 4. (a) Polarization curves at a scan rate of 5 mV s^{-1}, (b) Tafel plots, and (c) Nyquist plots of NF, NiFeOH/NF, CeO$_2$/NF-heat, and CeO$_2$-NiFeOH/NF. (d) Chronoamperometry measurements of long-term stability for 30 h at current densities of 10 mA cm^{-2} and 50 mA cm^{-2} for CeO$_2$-NiFeOH/NF.

For the NiFeOH/NF sample, a lower overpotential of 290 mV and an increased current density are obtained after doping Fe into NiOOH (shown in Figure 4(a)), which agrees with other studies that incorporate iron into NiOOH catalysts, which are intrinsically highly active for the OER [23-25, 40]. One reason for the improvement is that more OER active species, NiOOH, are formed on the surface, as shown by the XPS spectra. In addition, the doped Fe is in the form of Fe^{3+}. The presence of Fe^{3+} can also reduce the energy barrier to produce more NiOOH from Ni(OH)$_2$ during CV treatment [41]. As the LSV results for NiFeOH/NF and CeO$_2$-NiFeOH/NF show, there are oxidation peaks approximately 1.4 V, indicating that Ni(OH)$_2$ is electrooxidized to NiOOH. However, such a peak is not detected in the NF-heat or CeO$_2$/NF-heat samples. The other reason is that the doped Fe^{3+} plays an essential role in generating the NiOOH structure from NiO. NiOOH is the active site for OER. In addition, Fe^{3+} is important to stabilize the key active O radical intermediate during the OER to make the following chemical O-O coupling reaction proceed easier. Consequently, the onset potential of the OER decreases.

Moreover, doping Fe^{3+} can generate surface defects, which could have a partial-charge-transfer activation effect on Ni to enhance electrical conductivity of the catalysts, resulting in an increase in current density [42]. Thus, compared to NF-heat, adding Fe^{3+} dopants to form the NiFeOH/NF catalyst not only dramatically decreases the overpotential from 390 mV to 290 mV but also increases the current density by approximately 2.7 times at 2.0 V vs. RHE.

With the modification of both Fe^{3+} dopants and CeO_2 on NiOOH to form CeO_2-NiFeOH/NF, the lowest overpotential of 280 mV at 10 mA cm^{-2} is obtained, surpassing most reported non-noble-metallic OER catalysts (listed in Table S3). Specifically, a significant increase in the current density is more obvious when the potential is greater than 1.6 V. The current density of CeO_2-NiFeOH/NF can reach as high as 125 mA cm^{-2} at 1.7 V, whereas that of NiFeOH/NF is only 90 mA cm^{-2}. Such a current increase is more obvious than that between CeO_2/NF-heat and NF-heat. These results demonstrate that the OER activity of NiOOH is greatly enhanced by the co-modification of Fe^{3+} dopants and CeO_2 nanoparticles. When both Fe^{3+} dopants and CeO_2 nanoparticles are presented on the NiOOH surface, more oxygen vacancies are generated in the NiOOH structure than CeO_2/NF-heat, as detected by XPS. The oxygen vacancies can create defects, and the electrons in the defects are easily excited, resulting in improving the conductivity of CeO_2/NiFeOH-NF, which is also supported by density functional theory (DFT) calculations [43]. The presence of oxygen vacancies induces excess electron charge in the crystal, which is also supported by the lower BE shifts of NiO, $Ni(OH)_2$, and NiOOH in CeO_2/NiFeOH-NF based on the XPS results. Even though the oxidation states of Ni species in CeO_2/NiFeOH-NF are lower than those in the other three samples, more NiOOH species can be easily regenerated with Fe^{3+} dopants by CV treatment, which is proven by the presence of an anodic peak at 1.4 V of the LSV for CeO_2/NiFeOH-NF. Furthermore, the high conductivity of CeO_2/NiFeOH-NF is maintained. This conclusion can be further demonstrated by Nyquist plots. As presented in Figure 4(c), compared with all the samples investigated here, CeO_2-NiFeOH/NF shows the smallest charge transfer resistance (at high frequencies), the smallest reduction in mass-transfer resistance (at low frequencies) and the strongest electron interaction. Subsequently, the current density of CeO_2/NiFeOH-NF towards the OER is improved and the overpotential is reduced to 280 mV.

The Tafel plot is an important parameter to estimate the OER kinetics. As Figure 4(b) shows, CeO_2-NiFeOH/NF exhibited a Tafel slope of 32.1 mV dec^{-1}, which is much lower than those of NiFeOH/NF (42.8 mV dec^{-1}), CeO_2/NF-heat (58.9 mV dec^{-1}) and NF-heat (75.3 mV dec^{-1}). The lower Tafel slope indicates a faster reaction kinetic process for OER [44]. The Fe dopants in NiOOH not only reduce the energy barrier of NiOOH formation but also stabilize the active O radical intermediate. In addition, the formation of oxygen vacancies by introducing CeO_2 nanoparticles can improve the conductivity of the catalysts. Thus, the electroactivity of NF towards the OER is kinetically enhanced.

An ideal OER catalyst should not only have excellent activity but should also have outstanding stability over the long duration of water electrolysis. Since CeO_2-NiFeOH/NF shows the best activity, its stability for the OER was investigated by a long-term chronopotentiometry test, with the results displayed in Figure 4(d). Relatively steady operating potentials could be maintained at 1.52 V and 1.62 V for 30 hours under current densities of 10 mA cm^{-2} and 50 mA cm^{-2}, respectively, without visible increases. All results demonstrate that the CeO_2-NiFeOH/NF has excellent durability under higher current densities, which is beneficial for practical situations.

The electrochemical surface areas (ECSA) of the four samples studied here is determined by the non-faradaic electrical double-layer capacitance method, as reported in [34-35]. To estimate this area, cyclic voltammograms were recorded from -0.06 V to 0.06 V vs. Ag/AgCl with various scan rates in 1 M NaOH aqueous solution (the specific capacitance is 0.04 mF cm^{-2}), and the results are displayed in Figure S1. The ECSA of CeO$_2$-NiFeOH/NF, NiFeOH/NF, CeO$_2$/NF-heat, and NF-heat are 17.145 cm^2, 9.590 cm^2, 9.428 cm^2 and 8.349 cm^2, respectively. It is noted that an increment of approximately 2.05 times ECSA is obtained for CeO$_2$-NiFeOH/NF compared to NF-heat, indicating that the co-modification of Fe^{3+} dopants and CeO$_2$ nanoparticles to NiOOH can provide more surface area.

4. CONCLUSION

In summary, an efficient OER catalyst, CeO$_2$-NiFeOH/NF, was successfully synthesized by uniformly precipitating CeO$_2$ onto Fe^{3+}-doped NiOOH on nickel foam. As confirmed by the XPS results, the presence of Fe^{3+} dopants creates more NiOOH from NiO, and the addition of CeO$_2$ provides more oxygen vacancies in the NiOOH structure. The co-modification of Fe^{3+} dopants and CeO$_2$ generate the highest amount of oxygen vacancies in the NiOOH structure. The increasing amount of NiOOH enhances the electroactivity of the catalysts and reduces the overpotential for the OER. The oxygen vacancies in NiOOH improve the conductivity of the catalyst. Thus, the current density is increased. CeO$_2$-NiFeOH/NF with the highest amount of oxygen vacancies in the NiOOH structure exhibits the best catalytic activity and remarkable durability for the OER in alkaline solutions. In the future, such non-noble metallic catalysts and their feasible synthesis could be applied widely for water electrolysis.

SUPPORTING INFORMATION

Table S1 BE and concentrations of different nickel species obtained from core-level Ni 2p$_{3/2}$ XPS for NF-heat, CeO$_2$/NF-heat, NiFeOH/NF, and CeO$_2$-NiFeOH/NF.

	NF-heat		CeO$_2$/NF-heat		NiFeOH/NF		CeO$_2$-NiFeOH/NF	
component	BE/eV	at.%	BE/eV	at.%	BE/eV	at.%	BE/eV	at.%
NiO	854.2	41.55%	854.0	43.44%	854.9	5.53%	854.9	5.59%
Ni(OH)$_2$	855.9	42.54%	855.8	43.58%	856.4	48.43%	855.6	75.91%
NiOOH	857.4	15.91%	857.3	12.98%	857.8	46.04%	857.2	18.50%

Table S2 BE and concentrations of Ce compounds obtained from core-level Ce 3d$_{5/2}$ XPS for CeO$_2$, CeO$_2$/NF-heat, and CeO$_2$-NiFeOH/NF.

	CeO$_2$		CeO$_2$/NF-heat		CeO$_2$-NiFeOH/NF	
component	BE/eV	at.%	BE/eV	at.%	BE/eV	at.%
Ce^{4+}	882.8	75.48	882.5	78.12	882.5	91.72
Ce^{3+}	880.8	24.52	880.8	21.88	/	8.18

To perform quantitative analysis, the areas under the curve associated with the peaks were used. The total fraction of Ce^{3+} in CeO_2 was calculated according to the following equations:
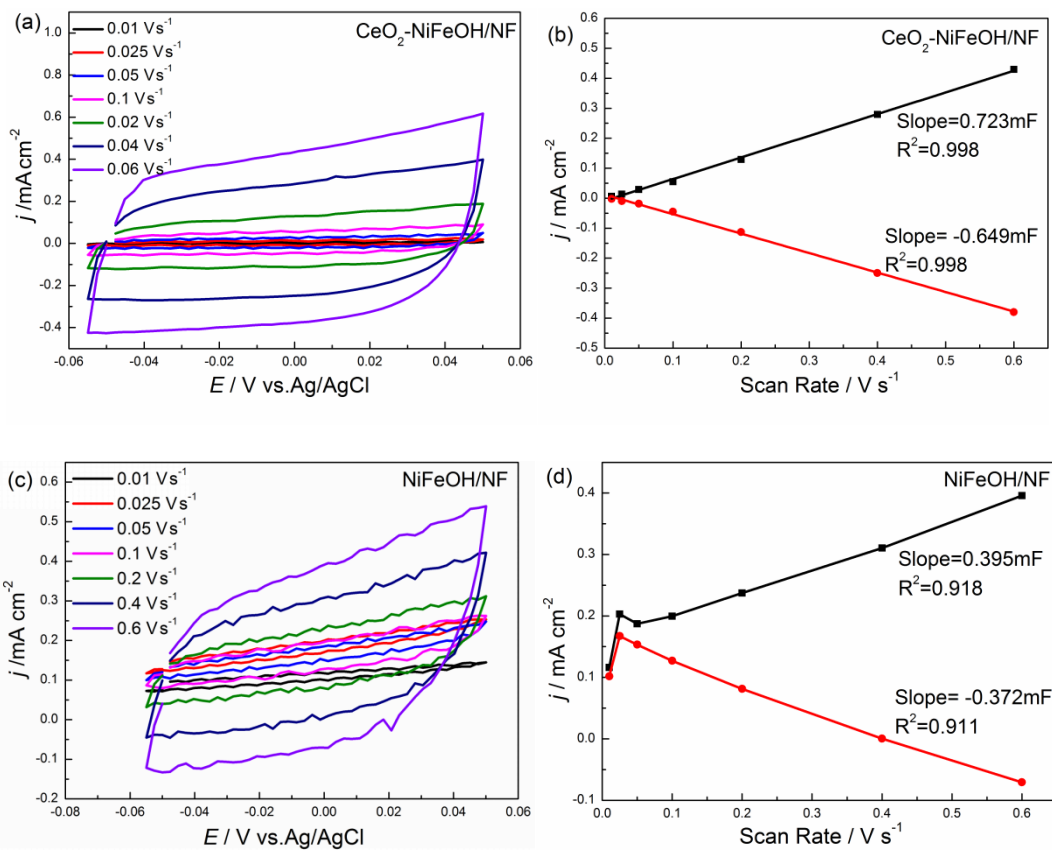
$$Ce(III) = U^0 + U' + V^0 + V' \qquad (1)$$

$$Ce(IV) = U + U'' + U''' + V + V'' + V''' \qquad (2)$$

$$Ce(III)\% \; from \; Ce \; 3d = \frac{Ce(III)}{Ce(III)+Ce(IV)} \qquad (3)$$

Table S3 Performance comparison of OER catalysts

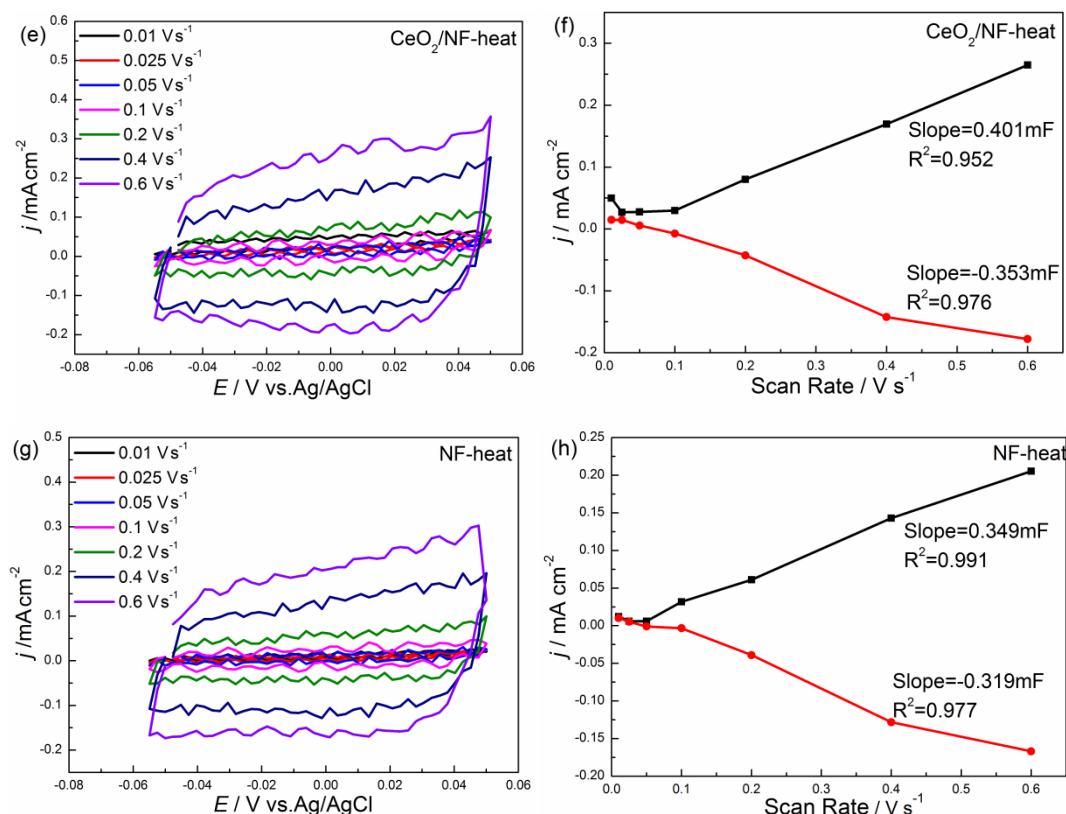| Catalyst	Overpotential / mV	Tafel / mV dec^{-1}	Reference
CeO_2-NiFeOH/NF	280	32.1	This work
NiO/NF	286	53	[45]
RuO_2 /NiO/NF	270	31.7	[46]
$W_{0.5}Co_{0.5-x}Fe_x$/NF	250	36	[47]
$Ni(OH)_2$/CNTs	270	33	[48]
Ni_2P	290	68.1	[49]
NiO_x	360	36	[50]
α-$Ni(OH)_2$	331	68	[51]
$NiCo_2O_4$	565	132	[52]
NiFe-LDH	320	57	[53]

Figure S1. Double-layer capacity measurement to determine the ECSA of CeO_2-NiFeOH/NF, NiFeOH/NF, CeO_2/NF-heat and NF-heat from CV scans in 1 M KOH. (a), (c), (e), and (g) are the CV plots measured in the non-Faradaic region of the voltammogram at the following scan rates: 0.01, 0.025, 0.05, 0.1, 0.2, 0.4 and 0.6 V s^{-1}. (b), (d), (f), and (h) are the cathodic (red line) and anodic (black line) charging currents measured at 0.00 V vs Ag/AgCl plotted as a function of scan rate.

Equations (4)-(5) are used to calculate C_{DL} and ECSA.

$$J_C = v * C_{DL} \qquad (4)$$

$$ECSA = C_{DL}/C_S \qquad (5)$$

in which Cs = 0.04 mF cm^{-2}.

For CeO_2-NiFeOH/NF as example, C_{DL} = (0.7226 - (-0.649))/2 = 0.6858 mF, ECSA(CeO_2-NiFeOH/NF) = C_{DL}/C_s = 0.6858/0.04 = 17.145 cm^2

References

1. C. C. L. McCrory, S. Jung, J. C. Peters, T. F. Jaramillo, *J. Am. Chem. Soc.,* 135 (2013) 16977–16987.
2. J. Greeley, T. F. Jaramillo, J. Bonde, I. Chorkendorff and J. K. Nørskov, *Nat. Mater.,* 5 (2016) 909–913.
3. A. J. Bard, L. R. Faulkner in *Electrochemical Methods: Fundamentals and Applications, Vol. 2,* John Wiley & Sons: New York, 2 (2001) 520-525.
4. Y. M. Lee, J. Suntivich, K. J. May, E. E. Perry and Y. S. Horn. *J. Phys. Chem. Lett.,* 3 (2012) 399–

404.

5. Y. Yin, S. Zhao, K. Zhao, M. Abdul, H. J. Tang, C. Lin, H. J. Zhao, G. Yan, Z. Y. Tang, *Nat. Commun.*, 6 (2015) 6430–6438.
6. J. Greeley, I. E. L. Stephens, A. S. Bondarenko, T. P. Johansson, H. A. Hansen, T. F. Jaramillo, J. Rossmeisl, I. Chorkendorff, J. K. Nørskov, *Nat. Chem.*, 1 (2009) 552–556.
7. J. Y. Liang, Y. Z. Wang, C. C. Wang. *J. Mater. Chem. A*, 4 (2016) 9797-9806.
8. J. L. Liu, Y. Zheng, Y. Jiao, S. Z. Qiao, *Small.* 14 (2018) 1704073-1704083.
9. L. C. Seitz, D. Nordlund, A. Gallo, T. F. Jaramillo, *Electrochimica. Acta.,* 193 (2016) 240-245.
10. Y. C. Pi, Q. Shao, P. T. Wang, X. Q. Huang, *Angew. Chem. Int. Ed.*, 56 (2017) 4502-4506.
11. L.Wang, H. Chen, Q. Daniel, L. C. Sun. *Adv. Energy Mater.*, 6 (2016) 1600516-1600521.
12. C. Xia, Q. Jiang, C. Zhao, M. N. Hedhili, H. N. Alshareef, *Adv. Mater.*, 28 (2016) 77−85.
13. M. Ledendecker, S. K. Calderón, C. Papp. *Angew. Chem.*, 127 (2015) 12538-12542.
14. A. J. Tkalych, H. L. Zhuang, E. A. Carter, *ACS Catal.*, 7 (2017) 5329−5339.
15. M. S. Burke, S. H. Zou, *J. Phys. Chem. Lett.*, 6 (2015) 3737−3742.
16. Q. Zhang, C. C. Zhang, J. B. Liang, P. G. Yin, Y. Tian, *ACS Sustainable Chem. Eng.*, 5 (2017) 3808−3818.
17. X. Li, G. Q. Han, Y. R. Liu, B. Dong, W. H. Hu, C. G. Li, *ACS Appl. Mater. Interfaces.*, 8 (2016) 20057−20066.
18. T. Tian, H. Gao, X. C. Zhou, L. R. Zheng, and Y. Ding, *ACS Energy Lett.*,3 (2018) 2150−2158.
19. R. Subbaraman, D. Tripkovic, K. C. Chang, D. Strmcnik, A. P. Paulikas, P. Hirunsit, M. Chan, J. Greeley, V. Stamenkovic, N. M. Markovic, *Nat. Mater.*, 11 (2012) 550−557.
20. O. D. Morales, D. F. Suspedra, M. T. M. Koper, *Chem. Sci.,* 7 (2016) 2639–2645.
21. Y. Yu, X. J. Yu, S. L. Yang, *J MATER SCI-MATER EL.,* 26 (2015) 5715–5723.
22. D. Sharma, B. R. Mehta, *Journal of Alloys and Compounds.,* 749 (2018) 329-335.
23. J. Qi, W. Zhang. *Adv. Sci.*, 2 (2015) 1500199-1500207.
24. L. Trotochaud, S. L. Young, J. K. Ranney, and S. W. Boettcher. *J. Am. Chem. Soc.*, 136 (2014), 6744−6753
25. O. D. Morales, I. L. Yanez, M. T. M. Koper, *ACS Catal.*, 5 (2015) 5380–5387.
26. Y. Yu, X. J. Yu, S. L. Yang, *J MATER SCI-MATER EL.*26 (2015) 5715–5723.
27. D. Sharma, B.R. Mehta, *Journal of Alloys and Compounds.,* 749 (2018) 329-335.
28. F. Esch, S. Fabris, L. Zhou, T. Montini, C. Africh, P. Fornasiero, G. Comelli, R. Rosei, *Science,* 309 (2005) 752–755.
29. J. X. Feng, S. H. Ye, H. Xu, Y. X. Tong, G. R. Li, *Adv. Mater.,* 28 (2016) 4698–4703.
30. Z. Q. Liu, N. Li, H. Y. Zhao, Y. Zhang, Y. H. Huang, Z. Y. Yin, Y. P. Du, *Chem. Sci.,* 8 (2017) 3211-3217.
31. S. Wang, J. Wu, J. Yin, Q. Hu, D. Geng, L.M. Liu, *ChemElectroChem*, 10 (2018).
32. Y. Hou, M. R. Lohe, J. Zhang, S. Liu, X. Zhuang, X. Feng, *Energy Environ. Sci.* 9 (2015) 478-483.
33. R. D. L. Smith, M. S. Prevot, R. D. Fagan, S. Trudel, C. P. Berlinguette, *J. Am. Chem. Soc.*, 135 (2013) 11580−11586.
34. Z. Wang, M. Li, L. Q. Fan, J. Han, Y. P. Xiong, *Applied Surface Science.*, 401 (2017) 89–99.
35. G. F. Dong, M. Fang, J. S. Zhang, R. J. Wei, *J. Mater. Chem. A*, 5 (2017) 11009-11015.
36. David R. Mullins, *Science Reports.,* 70 (2015) 42–85.
37. Z. Chen, C. X. Kronawitter, X. F. Yang. *Phys. Chem. Chem. Phys.,* 19 (2017) 31545-31552.
38. L. H. Sun, C. L. Yang, Y. Yuan. *INT J HYDROGEN ENERG., 4*2 (2017) 15140-15148.
39. E. A. Kulp, S. J. Limmer, E. W. Bohannan, J. A. Switzer, *Solid State Ionics.,* 178 (2007) 749-757.
40. M. W. Louie, A. T. Bell. *J. Am. Chem. Soc.,*135 (2013) 12329−12337.
41. Y. F. Li, A. Selloni. *ACS Catal.,* 4 (2014) 1148−1153.
42. H. Xiao, H.Y. Shin, W. A. Goddard. *PNAS.,* 115 (2018) 5872–5877.
43. V. Fidelsky, M. C. Toroker. *J. Phys. Chem. C.*, 120 (2016) 25405−25410.
44. Y. Q. Wang, B.H. Zhang, W. Pan. *ChemSusChem.,* 10 (2017) 4170–4177.

45. J. Y. Liang, Y. Z. Wang, C. C. Wang. J. *Mater. Chem. A,* 4 (2016) 9797-9806.
46. J. L. Liu, Y. Zheng, Y. Jiao, S. Z. Qiao, *Small.,* 14 (2018) 1704073-1704083.
47. Y. C. Pi, Q. Shao, P. T. Wang, X. Q. Huang, *Angew. Chem. Int. Ed.,* 56 (2017) 4502-4506.
48. L. Wang, H. Chen, Q. Daniel, L. C. Sun. *Adv. Energy Mater.,* 6 (2016) 1600516-1600521.
49. L. A. Stern, L. G. Feng, X. L. Hu. *Energy Environ. Sci.,* 8 (2015) 2347-2351.
50. K. Fominykh, J. M. Feckl, J. Sicklinger, M. Doeblinger, S. Boecklein, J. Ziegler, L. Peter, J. Rathousky, E.W. Scheidt, T. Bein, D. Fattakhova-Rohlfing, *Adv. Funct. Mater.,* 24 (2014) 3123-3129.
51. M. Gao, W. Sheng, Z. Zhuang, Q. Fang, S. Gu, J. Jiang, Y. Yan, *J. Am. Chem. Soc.,*136 (2014) 7077-7084.
52. H. Shi, G. Zhao, J. *Phys. Chem. C.,*118 (2014) 25939-25946.
53. M. Gong, Y. G. Li, H. L. Wang, Y. Y. Liang, J. Z. Wu, J. G. Zhou, J. Wang, T. Regier, F. Wei, H. J. Dai, *J. Am. Chem. Soc.,*135 (2013) 8452–8455.